

Large-deformation Analysis and Experimental Validation of a Flexure-Based Mobile Sensor Node

Jiajie Guo^a, Kok-Meng Lee^{*a}, *Fellow, IEEE/ASME*, Dapeng Zhu^b, Xiaohua Yi^b, Yang Wang^b

^a Woodruff School of Mechanical Engineering, Georgia Institute of Technology, Atlanta GA, 30332

^b School of Civil Engineering, Georgia Institute of Technology, Atlanta GA, 30332

Abstract— This paper presents a new magnetic wall-climbing car as a mobile sensor node (MSN) for health monitoring and dynamic testing of large civil (ferromagnetic) structures. Unlike traditional design where the distance between the front and rear wheel pairs is fixed, the electromagnetically driven compliant beam connecting the axles not only offers an effective means to negotiate corners when maneuvering on ferromagnetic surfaces, but also serves as a sensor attachment device. Specifically, this paper presents the design concept of a novel magnetic flexonic mobile node (FMN) incorporating a compliant beam and permanent magnets, and a two-dimensional model for simulating the deformed shape of the compliant beam. Simulation results show that there exist consistent relations between input/output displacements and rotation angle for control implementation in sensor attachment and corner negotiation regardless of gravity direction or the critical force for buckling. Experiment results are also provided to validate the theoretical model and compare with the analysis for sensor attachment and corner negotiation.

Index Terms— Flexible (mobile) robot, buckling, compliant mechanism, flexible structure, large deformation, constraint, sensor network.

I. INTRODUCTION

IN recent years, wireless sensor networks have attracted growing interest for the structural health monitoring (SHM) of civil structures [1]. The leap from traditional cable-based sensing systems to wireless sensor networks can significantly reduce installation time/cost, and potentially enable dense instrumentation and bring unprecedented improvements to structural monitoring. As another transformative change to sensor networks, the next revolution is predicted to be of mobile sensor nodes (MSNs) [2]. In a mobile sensor network, each MSN can be a sensor-carrying robot capable of autonomously exploring surroundings and exchange information with peers through wireless communication. Motivated by these emerging needs, this paper presents a

design method for developing flexure-based MSNs [3][4] for negotiating obstacles (such as corners, reinforced ridges) moving on ferromagnetic surfaces for SHM applications [5].

In general, three important factors in designing a wall-climbing robot are adherence, mobility and flexibility. In [6] the prototype robot was designed with suction cups for adherence to crawl on non-ferrous surfaces to inspect aircraft wings and fuselages. Using an induction pin, a magnetic wheeled robot can be easily detached by manipulating the magnetic flux direction [7]. For steel pipe inspection, a magnetic actuator incorporating with shape-memory-alloy coils has been developed to move in the complicated environment of pipes [8]. Most existing wheeled robots for similar applications are often designed and analyzed under small deformations to avoid nonlinearity of lateral bending and buckling. While designs based on rigid links/joints simplify analysis, they potentially limit the versatile functionality of a robot. To overcome this difficulty, multi-agent networks such as a self-assembly modular robot [9] provide a flexible architecture and relevant control methods for coordinated motions have been developed for multiple mobile robots [10][11]. This paper offers an alternative solution to design compliant structures allowing large deformation to provide flexible manipulation of a wall-climbing robot, and hence improves mobility and flexibility of an MSN for SHM. While illustrated in the context of a mobile sensor node, this design concept can potentially enhance the flexibility of existing modular robots.

Flexible mechanisms, such as joints and compliant mechanisms can be explored for such purpose. For example, an active pin joint is incorporated in a magnetic wheeled robot for internal piping inspection [12]. Various compliant mechanisms have also been studied for robot development, owing to the advantage of having no relative moving parts and thus no contact frictional dissipation [13][14][15][16][17]. For commanding robot movements through real-time feedback, control strategies have been developed based on various modeling methods [18], including rigid body motions [19][20][21], vibration modes [22], and finite element methods[23][24].

In many compliant mechanisms, flexible beams are used as a fundamental component. For a two-dimensional (2D) beam capable of large deflection under various load conditions, closed form solutions can be found in [25]; however, in terms of elliptic integrals, these solutions are computationally cumbersome for use in design and real-time control. More recently, a 3D beam model was developed in

Manuscript received October 1, 2010. (Write the date on which you submitted your paper for review.) The project is funded by the National Science Foundation, under grant number CMMI-0928095 (Program Manager: Dr. Shih-Chi Liu).

J. Guo and K.-M. Lee are with the George W. Woodruff School of Mechanical Engineering, Georgia Institute of Technology, Atlanta GA, 30332 USA (e-mail: kokmeng.lee@me.gatech.edu).

D. Zhu, X. Yi and Y. Wang are with School of Civil Engineering, Georgia Institute of Technology, Atlanta GA, 30332 USA (e-mail: yang.wang@ce.gatech.edu).

* Corresponding author.

[26] and solved through the multiple shooting method (MSM) [27][28]. Early work concerning the stability and buckling was motivated by structure design and analysis [29][30]. Given the instability nature of buckling, its occurrence is usually not desirable; as a result, most studies have been concentrated on the critical forces and load-displacement relation of buckling mechanisms [31]. With few exceptions (such as [32] where the post-buckling equilibrium was analyzed), very little work has been conducted on displacement relations in large deflection and buckling analysis of flexible beams.

This paper presents the design concept, model and analysis of a flexure-based-mechatronic (Flexonic) Mobile Node (FMN) [3][4] for maneuvering on ferromagnetic surfaces. In operation, the FMN utilizes large deflection and buckling of a compliant beam enabling it to flexibly negotiate different kinds of obstacles (such as abrupt angle changes) commonly encountered in complex civil structures. The remainder of this paper is organized as follows:

- With the applications such as [5] in mind, we present here the design concept of a novel magnet-wheeled FMN incorporating a flexible beam to achieve two important functions (sensor attachment and corner negotiation) with a simple mechanism. Besides designed to negotiate common obstacles encountered in complex civil structures, the compliant beam offers an effective means to attach/detach an accelerometer (onto or from the surface of a structure) for vibration measurements.
- A general quasi-static compliant beam model for simulating 2D beam deformation is then given. To exploit beam buckling for SHM applications, the work starts from a conventional viewpoint of load-displacement relation, and then evolves to the displacement-displacement relations. As will be shown, these forward and inverse models provide the essential basis for the design and control of a FMN.
- Performed on a prototype FMN developed at Georgia Tech [3], we then discuss experimental results demonstrating three loading scenarios for the compliant beam. The first validates the basic beam model under its own weight and a concentrated load. The second investigates the effect of gravity on the process of attaching a sensor of different weights. The third evaluates the FMN design by examining the torque provided by compliant beam for maneuvering around a corner on ferromagnetic surfaces.

II. DESIGN CONCEPT OF A FLEXONIC MOBILE NODE (FMN)

Figure 1 illustrates the design concept of an FMN, which consists of four independently driven magnetic wheels housed in two assemblies (front and rear) connected by a compliant beam. Unlike a rigid car frame with a fixed distance between the front and rear axles, the front axle of an FMN can be bent relatively to its rear axle by deforming the compliant beam (with both of its ends fixed on the two rigid bodies at P_0 and P_1). This enables the FMN not only to function as an agile locomotion but also a sensor loader.

In Fig. 1, OXYZ is a reference frame where X is parallel to the plane on which the FMN moves and points in its moving direction; and Z is normal to the plane. The local coordinate

frames, “xyz” and “ $\xi\eta\zeta$ ” (each with a subscript indicating its location along the beam path-length), are defined in the un-deformed and deformed configurations respectively. For examples, $x_0y_0z_0$ and $x_1y_1z_1$ are the local coordinate frames at and P_1 in the undeformed configuration, respectively. $P_s(x_s, y_s, z_s)$ and $Q_s(\xi_s, \eta_s, \zeta_s)$, represent the same material point to describe the beam shapes before and after deformation respectively, where the subscript s denotes the path-length normalized to the beam length L ($0 \leq s \leq L$); and u_s, v_s and w_s the nodal displacements along x_s, y_s and z_s axis directions respectively. All coordinates follow the right-hand rule with x_s and ξ_s assigned along the neutral axis of the beam, and z_s and normal to the beam surface.

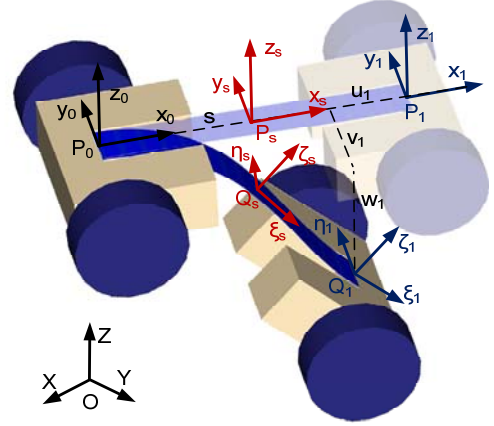


Fig. 1. Design concept and coordinate systems of a FMN.

Euler-Bernoulli beam theory is adopted to formulate the 2D large deformation behaviors of the beam subjected to specified forces, moments and constraints; both point and distributed external loadings are considered. For this, two assumptions are made: 1) the beam material is linear elastic. 2) Cross sections remain planar and normal to the reference axis after deformation. As an illustration, consider an element with length Δs in a compliant beam shown in Fig. 2(a). The element is subjected to two concentrated loads (F_1 and F_3) and a moment (M_2) as well as two external distributed loads (q_1 and q_3) and distributed moment (q_2), where the subscripts 1, 2 or 3 corresponds to the x, y or z (ξ, η or ζ) direction respectively. In Fig. 2(a), the concentrated loads and moment are presented in the deformed coordinates, $\xi_s\eta_s\zeta_s$; the external distributed loads and moment are in undeformed coordinates, $x_sy_sz_s$; and θ is the slope of the deformed beam shape.

A. Beam Deformation Model

Based on static analysis of a beam element, the equations for the force and moment equilibrium are given by (1a~ c):

$$-F_1 + (F_1 + \Delta F_1) \cos \Delta \theta + (F_3 + \Delta F_3) \sin \Delta \theta + q_1 \Delta s \cos \theta - q_3 \Delta s \sin \theta = 0 \quad (1a)$$

$$-F_3 + (F_3 + \Delta F_3) \cos \Delta \theta - (F_1 + \Delta F_1) \sin \Delta \theta + q_1 \Delta s \sin \theta + q_3 \Delta s \cos \theta = 0 \quad (1b)$$

$$-M_2 + M_2 + \Delta M_2 - (1+e)\Delta s(F_3 + \Delta F_3) + q_1 \Delta s^2 / 2 - q_3 \Delta s^2 / 2 + q_2 \Delta s = 0 \quad (1c)$$

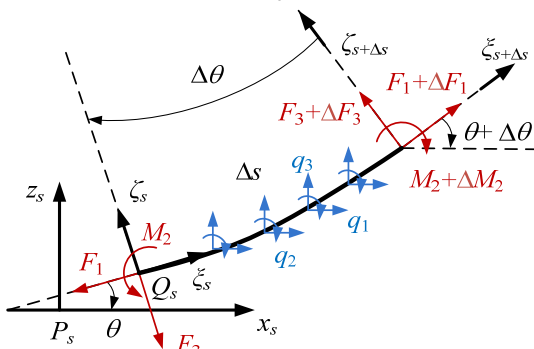
where e is the axial strain. For an infinitesimally small Δs ,

$\sin\Delta\theta \approx \Delta\theta$ and $\cos\Delta\theta \approx 1$. Neglecting higher order terms, (1a~c) can be rewritten in differential forms with respect to s :

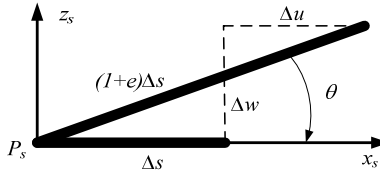
$$F_1' = -F_3\theta' - q_1 \cos \theta + q_3 \sin \theta \quad (2a)$$

$$F_3' = F_1\theta' - q_1 \sin \theta - q_3 \cos \theta \quad (2b)$$

$$M_2' = (1+e)F_3 - q_2 \quad (2c)$$



(a) Force and moment equilibrium.



(b) Displacements and orientation relations.

Fig. 2. Formulation of a beam model.

The element displaces as well as deforms as illustrated in Fig. 2(b), where Δs and $[(1+e)\Delta s]$ are the original and deformed element lengths, respectively. From Fig. 2(b), the nodal displacements and orientation can be obtained as

$$\frac{\Delta s + \Delta u}{(1+e)\Delta s} = \cos \theta \quad \text{and} \quad \frac{\Delta w}{(1+e)\Delta s} = -\sin \theta$$

These above relations can be rewritten in differential forms:

$$u' = (1+e) \cos \theta - 1 \quad (3a)$$

$$w' = -(1+e) \sin \theta \quad (3b)$$

Denoting $\theta' = \rho_2$ (3c)

(2) can be recast as $F_1' = -F_3\rho_2 - q_1 \cos \theta + q_3 \sin \theta$ (3d)

$$F_3' = F_1\rho_2 - q_1 \sin \theta - q_3 \cos \theta \quad (3e)$$

$$M_2' = (1+e)F_3 - q_2 \quad (3f)$$

where e and ρ_2 are given by

$$e = \frac{F_1}{EA} \quad \text{and} \quad \rho_2 = \frac{M_2}{EI} \quad (4a,b)$$

In (4), E is the elastic modulus; A is the cross section area; and I is the moment of inertia. In addition, the axial strain on the upper surface is given by

$$\varepsilon_{11} = e - \rho_2 h / 2 \quad (5)$$

where h is the beam thickness.

The boundary value problem (BVP) of the compliant beam can be written compactly in the following form:

$$\mathbf{X}' = \mathbf{f}(s, \mathbf{X}), \quad \mathbf{g}(\mathbf{X}(0), \mathbf{X}(1)) = \mathbf{0} \quad (6a,b)$$

where \mathbf{X} is a vector of the 6 variables $(u, w, \theta, F_1, F_3, M_2)^T$; $0 \leq s \leq l$; and $\mathbf{g}(\bullet)$ is the boundary conditions (BCs) specifying

geometrical and/or loading constraints at both ends. The BVP (6a, b) can be solved using a multiple shooting method (MSM) [27] given in Appendix, which recasts the BVP into an initial value problem (IVP).

B. Boundary Conditions

Appropriate boundary conditions must be specified to solve (3a~f) for the six unknowns in \mathbf{X} that are physically relevant. Table I summarizes four typical boundary conditions, which are also commonly specified for analyzing columns. For a cantilever (Type 1) where the slope and displacements are zeros at the fixed end, the forces and moment at the free end must be specified. For a beam with both ends constrained with pin-joints (Type 2), the displacement constraints cannot sustain any moment; $M_2 = 0$ but F_1 must be specified. As will be illustrated, Types 3 and 4 are specified for sensor attachment and for negotiating a convex corner, respectively. Type 3 is similar to Type 2 but can resist nonzero moments while maintaining zero slopes at both ends. In Type 4, a nonzero moment can be exerted against an offset pinned end. Unlike buckling analyses where the critical load causing a column to buckle is of particular concern, the models developed here relax several commonly made ideal-beam assumptions (such as mass-less and small deflection) for practical FMN applications.

C. Illustrative Examples

The beam model is best illustrated by numerically simulating the two basic functions of an existing FMN [5] where a compliant beam connects the front and rear axles of the FMN (Fig. 1).

- The 1st function attaches or detaches an accelerometer on/from the surface to be measured. The compliant beam is normally straight. When a measurement is to be made, the front axle is driven towards the rear axle to buckle the compliant beam allowing the accelerometer to be pressed against the surface to be measured.
- The 2nd function provides a means to overcome obstacles when moving on a structure. Among the challenges is negotiating sharp corners. Magnetic forces at the corner greatly decrease when negotiating a convex corner, but increase (because of multiple contacts) when moving up or down a concave corner.

As illustrated in Fig. 3(a), the FMN consists two U-shaped structural frames on which the motors and electronics are housed and a spring steel (0.254mm thick) laminate including a compliant beam (shaded in gray). The non-shaded portions are fastened by screws onto the U-shaped frames. The accelerometer (50 grams) is pinned in the middle of the beam by screws (at locations shaded in black). The geometrical and mechanical properties of the compliant beam are given in Fig. 3(b). The beam has non-uniform cross-sections; thus A and I are functions of s . Figure 3(c) shows a steel (A36) structure as the working environment, where the FMN will cross the corner A and attach a sensor at B and C.

TABLE I
BOUNDARY CONDITIONS FOR GENERALIZED CONSTRAINTS

| Type | 1. Cantilever | 2. Both ends pinned | 3. Slide against a fixed end | 4. Slide against an offset pinned end |
|-------|----------------------|-----------------------|------------------------------|---------------------------------------|
| | | | | |
| $s=0$ | $\theta = u = w = 0$ | $M_2 = 0, u = w = 0$ | $\theta = u = w = 0$ | M_2, u, w |
| $s=L$ | F_1, F_3, M_2 | $F_1, M_2 = 0, w = 0$ | $F_1, \theta = w = 0$ | $F_1, \theta = w = 0$ |

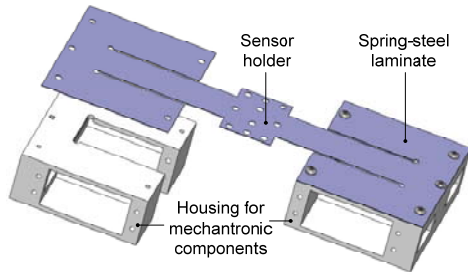
Numerical simulations using MSM were performed, where computation time (especially when there is buckling) depends on the number of segments, N , and initial values for the process. The MSM computation involves a $6(N+1) \times 6(N+1)$ matrix inverse. To reduce computation time, the beam is equally divided into three segments ($N=3, m=4$ in Fig. A) with the beam cross-sectional area presented as a piecewise linear function of path length. As given in Table I, some of the initial values are zeros. The remaining nonzero initial values are determined by physics. Consider a cantilever as an illustration, the values of F_1 and F_3 at $s = 0$ can be obtained from equilibrium; and M_2 can be chosen as the multiplication of the forces by a characteristic length (such as one half of the beam length).

Example 1: Sensor attachment

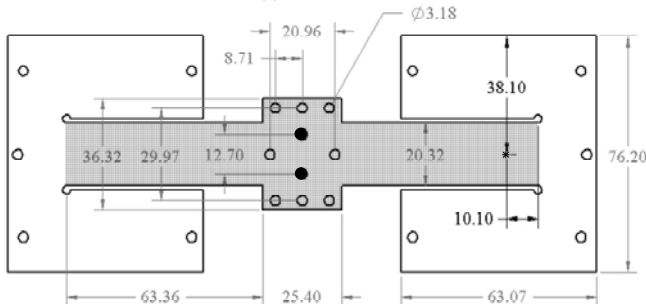
In modeling the sensor attachment on a plane, the rear axle is treated as a fixed end, and the front axle acts as a slider subjected to a uni-axial loading F_1 as shown in Fig. 4. In addition, it is assumed that the compliant beam is constrained to bend only in the $-z$ direction. For a given wheel radius, the uni-axial loading F_1 required to move the sensor to its desired displacement w_s (at $s = L/2$) depends on the direction of the sensor displacement relative to gravity as compared in Fig. 4, which compares two cases. Unlike Case 1 where the weights of the sensor and beam facilitate the sensor attaching, the beam must compensate for these weights in Case 2. To explain the effect of the gravity, we normalize the specified F_1 to the critical buckling force for a beam subjected to both ends fixed [33] as follows:

$$n = F_1 \left(\frac{4L^2}{\pi^2 EI_n} \right) \quad (7)$$

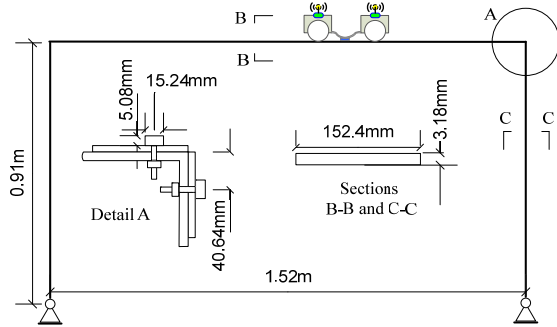
where I_n is the moment of inertia for the narrowest section (width=20.32mm in Fig. 3) of the beam; L is the beam length. For the sensor, the gravity normalized using (7) is about 0.8. With Type 3 BCs, the deformed shape (or w as a function of path length s) and u_1 for specified F_1 can be computed by solving the BVP (6). The results for the two cases (with $\varphi=0$) are compared in Figs. 4 and 5 where n varies from 0 to 25.



(a) CAD model.

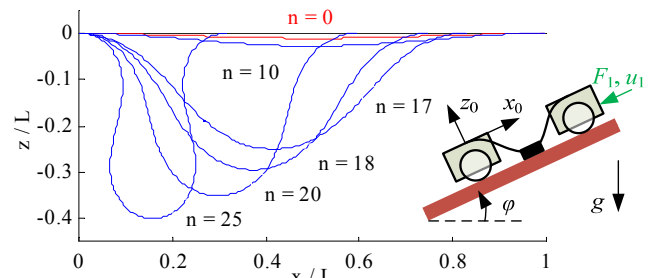


(b) Spring-steel laminate. ($E=207\text{GPa}$; $G=79.3\text{GPa}$; Poisson ratio=0.3; Density= 7.63g/cm^3 ; Thickness= 0.254mm)

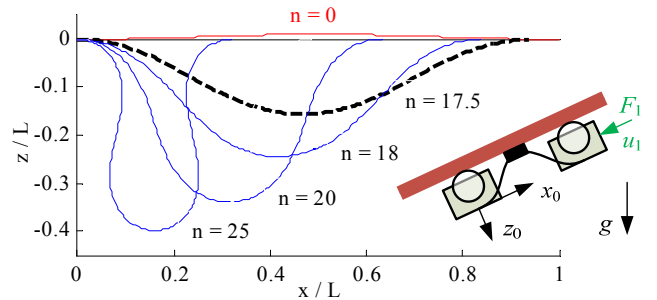


(c) Steel (A36) frame structure.

Fig. 3. CAD model of compliant structure for a magnetic FMN.



(a) Case 1, $\varphi = 0$.



(b) Case 2, $\varphi = 0$.

Fig. 4. Effect of gravity.

Some observations are discussed as follows:

- Figs. 4(a) and 5(a) show that the beam deforms continuously as the normalized force increases in Case 1.
- Although the carrying mass (50 gram sensor) is relatively light causing negligible deformation under its own weight (red curves in Fig. 4, $F_1=0$), this little weight however has a significant buckling effect on the beam in Case 2. As illustrated in Figs. 4(b) and 5(a), both the displacements (u_1 and w_s) in Case 2 do not change until the normalized force exceeds a critical value n_c at which the beam buckles drastically to a new shape (black dash curve in Fig. 4b) without any intermediate shapes. The values of u_1 and w_s , which correspond to n_c for $\varphi=0^\circ, 45^\circ, 90^\circ$, are summarized in Table II, which also shows the effects of sensor weights on these values. These critical value that causes buckling to set off in Case 2 decreases (requiring less compensation against gravity) as φ increases. For the same reason, a heavier weight tends to give rise to a larger critical value for $\varphi < 45^\circ$. On other hand, a smaller critical value for a lighter weight for $\varphi > 45^\circ$ is observed as gravity facilitates buckling.
- For $\varphi = 90^\circ$, the theoretical value of 16 given in [33] for a weightless beam is somewhat larger than n_c of 15.5. The beam model given in (3a~f) accounts for the gravity along $-x$, which contributes to the onset of buckling.
- The values of w_s for different φ values converge to the case $\varphi = 90^\circ$ for large F_1 when the gravity becomes negligible. This is also true for u_1 because of the monotonous relation between w_s and u_1 as shown in Fig. 5(b). The maximum normalized force required is $n=25$, from which the required motor torque can be estimated by multiplying F_1 computed from (7) by the wheel radius r_w .
- The solution to the beam model provides two alternative manipulating variables (F_1 or u_1) of controlling w_s for attaching a sensor. As illustrated in Fig. 5(a), the relationship between F_1 and w_s is not only highly nonlinear but also depends on φ . On the other hand, the relationship between w_s and u_1 is monotonically smooth and independent of φ as shown in Fig. 5(b). Thus, it is a preferable variable for controlling the compliant beam of the FMN by manipulating the input displacement u_1 rather than the input force F_1 . For the compliant design given in Fig. 3, the inverse model that computes u_1 for a specified w_s for attaching sensor is given by curve-fitting the data in Fig. 5(b) for different φ 's in both cases:

$$u_1 / L = 18(w_s / L)^3 + 5.3(w_s / L)^2 - 0.85w_s / L \quad (8)$$

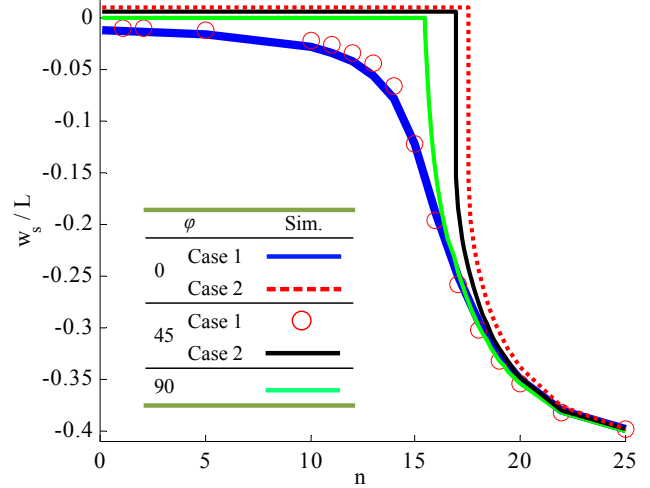
This result is due to the light weight of the combined beam and sensor. For detaching a sensor, the command becomes $-u_1$ for a reversed process.

Example 2: Convex corner negotiation

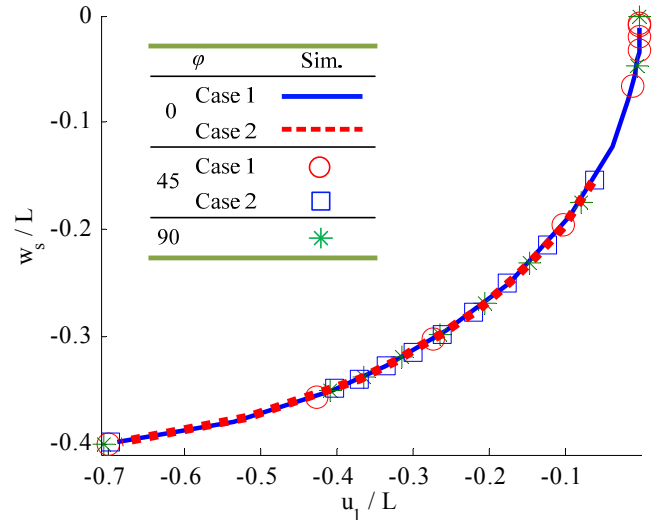
Figure 6 shows the free body diagram of the front assembly (mass m_1 at mass center C_1 and wheel radius r_w) at an instant crossing a convex corner A. The reference OXYZ is defined such that X is on the plane where the FMN initially locates points in the moving direction before crossing the corner; and is normal to the plane. In Fig. 6, ψ is the angle between Z and the gravity; N is the reaction force; and $f (= \mu N)$ is the friction;

is the coefficient of friction between the wheel and surface; M_m is the torque provided by the motors. The following assumptions are made in this discussion:

- 1) The wheels are designed with magnets such that they attach on the steel surfaces as the FMN moves.
- 2) The motor torque satisfying the non-slip condition: $M_m = f r_w \leq \mu N(\alpha) r_w$
- 3) The moment due to the magnets is small as compared to that due to gravity and thus neglected in the analysis.



(a) Relation between force n and displacement w_s/L .



(b) Relation between u_1 and w_s .

Fig. 5. Relationship between normalized force and displacements.

TABLE II
SLOPE ANGLE AND CRITICAL VALUES

| Sensor mass (gram) | φ (degree) | n_c | u_1 / L | w_s / L |
|--------------------|--------------------|-------|-----------|-----------|
| 50 | 0 | 17.5 | -0.0624 | 0.1559 |
| | 45 | 16.9 | -0.0612 | 0.1543 |
| | 90 | 15.5 | -0.0002 | 0.0094 |
| 100 | 0 | 18.3 | -0.0999 | 0.1948 |
| | 45 | 17.3 | -0.1069 | 0.2009 |
| | 90 | 15.1 | -0.00005 | 0.0001 |

The following discussion considers a worst scenario where the wheel has a point contact at the corner. The strategy for an FMN to negotiate a convex corner comprises three steps:

one U-shape frame for fixation) so that the complexities of the front and rear assemblies can be avoided.

- 2) The second is to investigate the effect of gravity on sensor attachment by comparing simulations for the structure at $\varphi = 0$ and 90° (Fig. 5(b)) against those obtained experimentally. The comparison also provides a basis for validating (8) that relates the displacement w_s (for attaching a sensor) to the input displacement u_1 .
- 3) The third objective is to examine the effectiveness of the proposed strategy for crossing a corner. Of particular interest is to determine the required input displacement u_0 for a desired rotation angle α as shown in Fig. 7.

For quantitative comparison, experimental results of the sensor attachment and corner negotiation processes were computed from images filmed by a camcorder (Sony HDR-SR11).

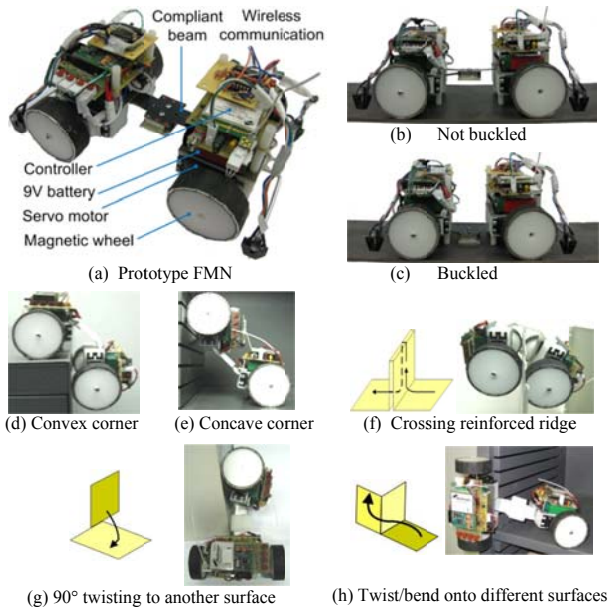


Fig. 9. Prototype FMN.

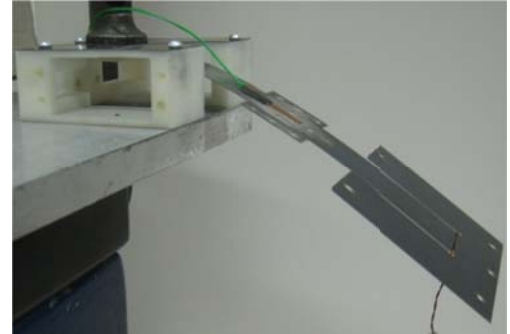
A. Validation of the beam model

Figure 10(a) shows the experimental setup to examine the validity of the beam model, where the spring-steel laminate on one of two housing structures (Fig. 3(a)) was clamped as a cantilever, and thus has Type 1 constraints (Table I). The remaining U-shaped portion (non-shaded in Fig. 3(b)) in the spring-steel laminate serves as a load at the end of the compliant beam (that has a non-uniform shape and thus non-uniform distributed weight). As the mass center of this U-shaped portion is located at 10.1mm from the free end of the beam (Fig. 3(b)), the weight of this U-shaped portion also contributes to a lateral force F_U and a moment M_U in addition to the external payload m_p at the free end of the beam. As a result, the values of F_1 , F_3 and M_2 in the boundary conditions are given by

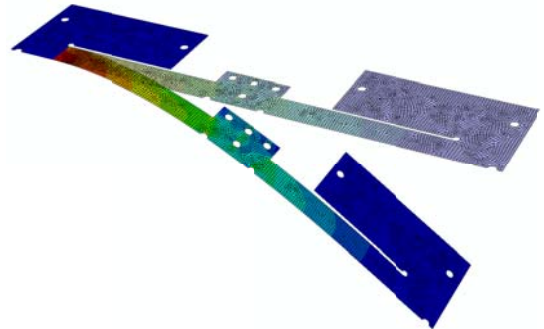
$$F_1 = 0, F_3 = F_U + m_p g, M_2 = M_U \quad (13)$$

In this experiment, a strain gauge (with negligible weight as compared to the beam) was attached on the upper surface at middle of the beam. To provide an alternative basis for comparisons, a numerical model was built in Abaqus using

6319 shell elements (S4R type). In FE analysis, only one-half of the beam is simulated because of symmetry, and the load is applied at one coupling element so that F_U is uniformly distributed over the cross section at the beam tip. All computations were performed on a computer with a 2.99 GHz CPU and 4.00GB memory; the FEM took about 365 seconds while the beam model (3-segment MSM) requires only 95 seconds. The results are given in Fig. 11 which compares the results of two beam models, uniform width of 20.32mm and non-uniform shape (that accounts for the geometry of the sensor holder), against those of FEM and experiment.



(a) Experiment setup.



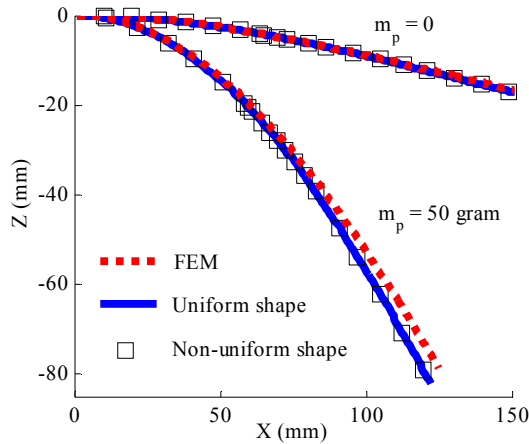
(b) Finite element analysis.

Fig. 10. Validation of beam model.

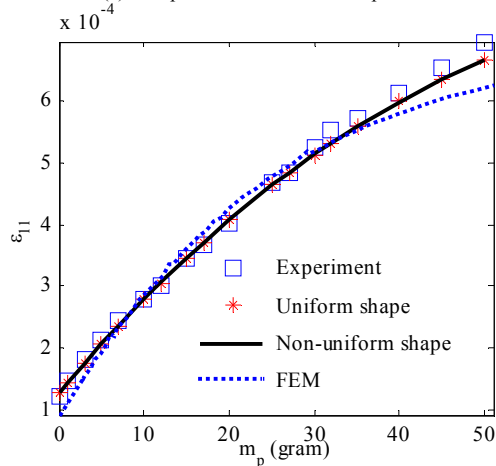
The results are discussed as follows:

- Figure 11(a) shows that the FEM computed beam-shapes and the uniform/non-uniform beam models closely agree with each other for two different loadings; external payload $m_p = 0$ and 50 gram exerted at the beam tip.
 - Figure 11(b) shows that the strain ε_{11} increases monotonically with payload. The beam model agrees well with the experimental measurements. Some discrepancies at large payloads are observed in FEM possibly due to the following local effects:
 - a. Because of FE meshes, the node at which strain information is extracted does not locate exactly at the middle of the beam.
 - b. Besides, the FEM model can capture the local stress concentration while the strain gauge is actually measuring the average strain over its area, and the stress concentration is not accounted in this beam model. When comparing this local information, the beam model matches with experiments but some discrepancy exists in the FEM.
- It is noted that the ten-hole area takes up to 8% of that of sensor holder, which was compensated for by a function

characterizing the change in beam widths; thus the results two beam models, uniform and non-uniform shapes, do not differ significantly in this specific application.



(a) Comparison of deformed shapes.

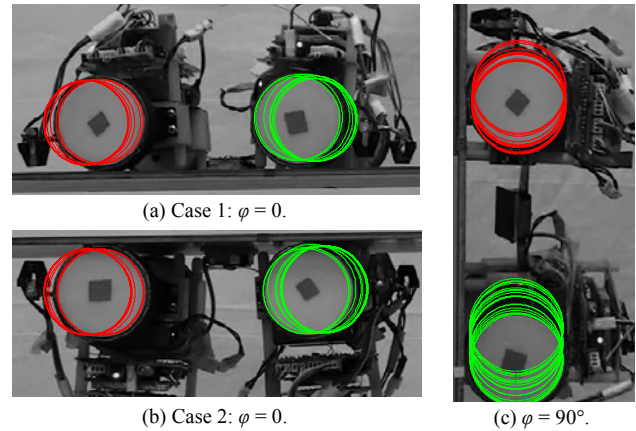
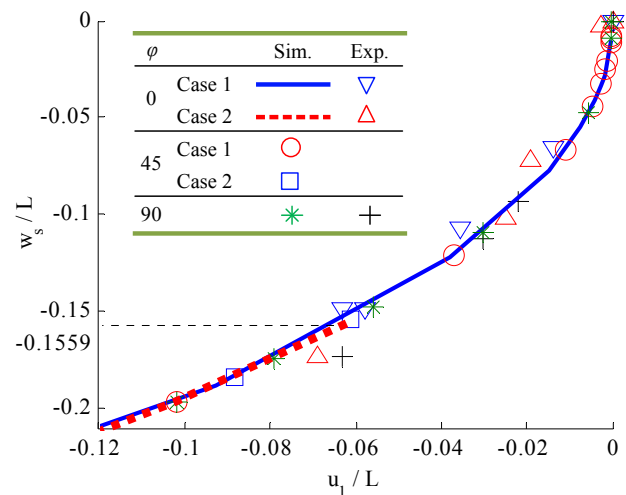
(b) Comparison of upper-surface strains at the middle of the beam.
Fig. 11. Comparison of results.

B. Effect of gravity on sensor attachment

In this experiment, the sensor was attached on the plane by moving both axles towards each other to prevent slippage as shown in Fig. 12(a-c). For comparing against analytical simulations where sensor attachments were modeled as a process of moving the front axle towards the fixed rear axle, the net displacement u_1 was obtained by measuring the distance change between the front and rear wheel centers from captured images.

Figure 12(d) is a zoom-in comparison of Fig. 5(b) showing good agreements between analyses and experiment results for $\varphi = 0, 45^\circ$ and 90° . It is worth noting that the deviation in Case for $\varphi = 0$ was a result due to the onset of buckling; once the critical force is overcome, w_s/L jumps from zero to -0.1559 . This non-linear dynamic is essentially unstable. Thus, in Case 2, the required input displacement u_1 for $w_s/L > -0.1559$ is of the same value ($u_1/L = -0.06$) as that when buckling starts. However, all the intermediate experiment data follows the continuous curve given by (8) which is independent of slope angle φ , so the relation between u_1 and w_s obtained from static

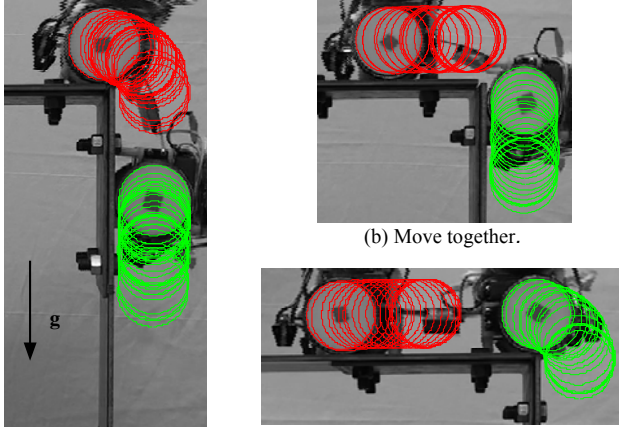
analysis is also valid for the dynamic process of Case 2. This also justifies for the conclusion obtained from Fig. 5 to control the compliant beam deformation by manipulating the input displacement u_1 rather than the input force F_1 .

(a) Case 1: $\varphi = 0$.(b) Case 2: $\varphi = 0$.(c) $\varphi = 90^\circ$.(d) Displacement comparison between simulation and experiment.
Fig. 12. Sensor attachment.

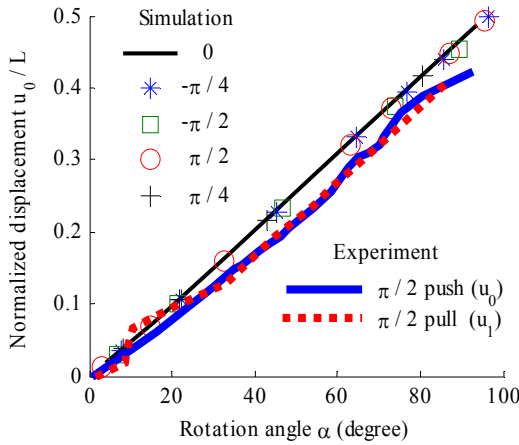
C. Validation of the corner negotiation

Figure 13(a-c) shows the three steps in negotiating a convex right corner by pushing the front axle, both axles moving together and finally pulling the rear axle. Following the analysis before, the rotation angle α of the front axle is by the orientation of the line connecting the front wheel center and the corner point, while the displacement u_0 of the rear axle is determined by the rear wheel center. Although the relation between the applied force F_1 and the desired rotation angle α nonlinear depending on the gravity direction, a highly linear relation $u_0/L = 0.0051\alpha$ exists between u_0 and α regardless of the gravity direction in simulation as shown in Fig. 13(d). Experiment results also confirm with this linear relation. It is noted that errors may come from the required torque that is calculated from the assembly mass and the distance from the corner to the mass center. Another source of error can be the image processing of the video frames when detecting the front and rear axle locations by wheel centers, and determining the corner point by manually picking one pixel. Since the steel structure and the camcorder are fixed throughout the experiment, this corner point A is fixed in all the images while

small vibration can exist in the steel structure because of the FMN dynamics. It can also be seen that both the pushing and pulling process follows the same curve in experiment, the above analysis for the pushing process (Step 1) can be applied throughout the corner negotiation.



(a) Push the front axle. (b) Move together. (c) Pull the rear axle.



(d) Relation between rotation angle α and displacement u_0/L .
Fig. 13. Convex right corner negotiation.

IV. CONCLUSION

Along with an analytical model for simulating the large deformation of a compliant beam in 2D space, a magnetic flexonic mobile node (FMN) incorporating a compliant mechanism has been designed to negotiate corners and carry a sensor for placing on a ferromagnetic structure. Two examples of sensor attachment and corner negotiation are presented for different constraints for the same mechanical design of FMN. Simulation results show that there exist consistent relations between input/output displacements and rotation angle for control implementation in sensor attachment and corner negotiation regardless of gravity direction. In attachment, a nonlinear relation between the front assembly displacement and the sensor displacement is valid for different critical forces for buckling which is affected by the working surface slope. In corner negotiation, a linear relation can be obtained between the displacement of the rear assembly and

rotation angle of the front assembly within the highly load-displacement behaviors of a compliant beam. However, the gravity affects the loading and displacement/rotation angle relation. To set off the beam buckling for the sensor the smaller the surface slope angle is, the larger the critical force is needed; a heavier sensor weight tends to give rise to a larger critical force for slope angle $\varphi \leq 45^\circ$ while smaller force for $\varphi > 45^\circ$. For a desired rotation angle in corner negotiation, a larger pushing force is required with a larger angle ψ between the gravity and the norm of the initial plane. The analytical model is validated by an experiment on a cantilever beam and the corresponding finite element model. Finally, the experimental results of two functionalities of attachment and corner negotiation are provided to validate the simulation analysis.

APPENDIX

MULTIPLE SHOOTING METHOD (MSM)

The boundary condition problem (BVP) of a 2D compliant beam can be written in the following form:

$$\mathbf{X}' = \mathbf{f}(s, \mathbf{X}), \quad \mathbf{g}(\mathbf{X}(0), \mathbf{X}(L)) = \mathbf{0} \quad (\text{A.1})$$

where \mathbf{X} is a vector of the 6 variables; $0 \leq s \leq L$; and $\mathbf{g}(\bullet)$ is the boundary conditions (BCs) specifying the geometrical loading constraints at both ends. The BVP (A.1) is recast as an initial value problem (IVP) and solved using a MSM [27]. For this, the region $[0, L]$ is divided into $m-1$ sections by m nodes as shown in Fig. A, where s_i is the arc length from the root of the beam to the i^{th} node; $\mathbf{x}_i^{(n)}$ is the initial guesses for the i^{th} section, and the superscript (n) denotes the n^{th} guess.

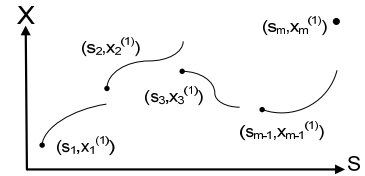


Fig. A. Multiple shooting method.

The BVP can then be posed as a set of m 1st-order non-linear equations (A.2) subject to a set of m constraints (A.3) as functions of the initial guesses:

$$\mathbf{X}' = \mathbf{f}(s, \mathbf{X}), \quad \mathbf{X}(s_i) = \mathbf{x}_i^{(n)} \quad (\text{A.2})$$

$$\mathbf{C}(\mathbf{x}^{(n)}) := \begin{bmatrix} \mathbf{C}_1(\mathbf{x}_1^{(n)}, \mathbf{x}_2^{(n)}) \\ \vdots \\ \mathbf{C}_{m-1}(\mathbf{x}_{m-1}^{(n)}, \mathbf{x}_m^{(n)}) \\ \mathbf{C}_m(\mathbf{x}_1^{(n)}, \mathbf{x}_m^{(n)}) \end{bmatrix} := \begin{bmatrix} \mathbf{X}(s_2; s_1, \mathbf{x}_1^{(n)}) - \mathbf{x}_2^{(n)} \\ \vdots \\ \mathbf{X}(s_m; s_{m-1}, \mathbf{x}_{m-1}^{(n)}) - \mathbf{x}_m^{(n)} \\ \mathbf{g}(\mathbf{x}_1^{(n)}, \mathbf{x}_m^{(n)}) \end{bmatrix} \quad (\text{A.3})$$

Using Newton method, the initial guesses are updated using (A.4):

$$\mathbf{x}^{(n+1)} = \mathbf{x}^{(n)} - \alpha [DC(\mathbf{x}^{(n)})]^{-1} \mathbf{C}(\mathbf{x}^{(n)}), \quad n = 0, 1, \dots \quad (\text{A.4})$$

where $DC = \partial \mathbf{C} / \partial \mathbf{x}^{(n)}$ is a matrix, α is a coefficient for the iteration step size. The iteration process of (A.4) stops until $\mathbf{C}(\mathbf{x}^{(n)}) \rightarrow \mathbf{0}$ (or a small tolerance error Err_{tol}) implying that the solution is continuous and satisfies the BCs. The MSM can be implemented using the following steps:

1. Set the initial guess $\mathbf{x}^{(0)} = [\mathbf{x}_1^{(0)} \quad \mathbf{x}_2^{(0)} \quad \dots \quad \mathbf{x}_m^{(0)}]$.
2. Solve the IVP (9a) with $\mathbf{X}(0) = \mathbf{x}^{(0)}$.
3. Calculate the residual $\|\mathbf{C}(\mathbf{x}^{(0)})\|$ and corresponding $DC = \partial \mathbf{C} / \partial \mathbf{x}^{(0)}$.
4. Update the initial guess by (A.4).
5. Repeat steps 2~4 (replacing $\mathbf{x}^{(0)}$ with $\mathbf{x}^{(n)}$) until $\|\mathbf{C}(\mathbf{x}^{(n)})\| < \text{tolerance error } Err_{tol}$.

ACKNOWLEDGMENT

The project is funded by the National Science Foundation, under grant number CMMI-0928095 (Program Manager: Dr. Shih-Chi Liu) and, in part, by the Agricultural Technology Research Program.

REFERENCES

- [1] J. P. Lynch and K. J. Loh, "A summary review of wireless sensors and sensor networks for structural health monitoring," *Shock and Vibration Digest*, vol. 38, pp. 91-128, 2006.
- [2] I.F. Akyildiz, W. Su, Y. Sankarasubramaniam, and E. Cayirci, "A survey on sensor networks," *IEEE Commun. Mag.*, vol. 40, no. 8, pp. 102-144, 2002.
- [3] K.-M. Lee, Y. Wang, D. Zhu, J. Guo, and X. Yi, "Flexure-based mechatronic mobile sensors for structure damage detection," *Proc. of the 7th Int. Workshop on Structural Health Monitoring*, Stanford, CA, 2009.
- [4] J. Guo, K.-M. Lee, D. Zhu, and Y. Wang, "A flexonic magnetic car for ferro-structural health monitoring," *Proc. of 2009 ASME Dynamic Systems and Control Conference*, Hollywood CA, 2009.
- [5] D. Zhu, X. Yi, Y. Wang, K.-M. Lee, and J. Guo, "A mobile sensing system for structural health monitoring: design and validation," *Smart Mater. Struct.*, vol. 19, 055011, 2010.
- [6] J.Z. Shang, T. Sattar, S. Chen, and B. Bridge, "Design of a climbing robot for inspecting aircraft wings and fuselage," *Int. J. of Industrial Robot*, vol. 34, pp. 495-502, 2007.
- [7] S.C. Han, J. Kim, and H.C. Yi, "A novel design of permanent magnet wheel with induction pin for mobile robot," *Int. J. of Precision Engineering and Manufacturing*, vol. 10, no. 4, pp. 143-146, 2009.
- [8] H. Yaguchi and N. Sato, "Globular Magnetic Actuator Capable of Free Movement in a Complex Pipe," *IEEE Trans. on Magnetics*, vol. 46, no. 6, pp. 1350-1355, 2010.
- [9] H. Wei, Y. Chen, J. Tan, and T. Wang, "Sambot: A Self-Assembly Modular Swarm Robot System," *IEEE/ASME Trans. on Mechatronics*, DOI 10.1109/TMECH.2010.2085009, Nov. 11, 2010.
- [10] S. Liu, D. Sun, and C. Zhu, "Coordinated Motion Planning for Multiple Mobile Robots Along Designed Paths With Formation Requirement." *IEEE/ASME Trans. on Mech.*, DOI 10.1109/TMECH.2010.2070843, Sept. 23, 2010.
- [11] H. Mehrjerdi, M. Saad, and J. Ghommam, "Hierarchical Fuzzy Cooperative Control and Path Following for a Team of Mobile Robots." *IEEE/ASME Trans. on Mech.*, DOI 10.1109/TMECH.2010.2054101, July 23, 2010.
- [12] F. Tâche, W. Fischer, G. Caprari, R. Siegwart, R. Moser, and F. Mondada, "Magnebike: A Magnetic Wheeled Robot with High Mobility for Inspecting Complex Shaped Structures," *J. of Field Robotics* vol. 26, pp. 453-476, 2009.
- [13] M. Filipovic, and M. Vukobratovic, "Expansion of source equation of elastic line," *Robotica*, vol. 26, pp. 739-751, 2008.
- [14] J.G. Garcia, A. Robertsson, J.G. Ortega, and R. Johansson, "Sensor Fusion for Compliant Robot Motion Control," *IEEE Trans. on Robotics*, vol. 24, no. 2, pp. 430 - 441, 2008.
- [15] U.-X. Tan, W. T. Latt, C.Y. Shee, and W.T. Ang, "A Low-Cost Flexure-Based Handheld Mechanism for Micromanipulation." *IEEE/ASME Trans. on Mechatronics*, DOI 10.1109/TMECH.2010.2069568, Sept. 27, 2010.
- [16] C.-C. Lan, C.-M. Lin, and C.-H. Fan, "A Self-Sensing Microgripper Module with Wide Handling Ranges." *IEEE/ASME Trans. on Mechatronics*, DOI 10.1109/TMECH.2009.2037495, Jan. 8, 2010.
- [17] H. Xie and S. Regnier, "Development of a Flexible Robotic System for Multiscale Applications of Micro/Nanoscale Manipulation and Assembly." *IEEE/ASME Trans. on Mechatronics*, DOI 10.1109/TMECH.2010.2040483, Feb. 8, 2010.
- [18] S.K. Dwivedy, and P. Eberhard, "Dynamic analysis of flexible manipulators, a literature review," *Mechanism and Machine Theory*, vol. 41, no. 7, pp. 749-777, 2006.
- [19] M.A. Arteaga, and B. Siciliano, "On tracking control of flexible robot arms," *IEEE Trans. on Automatic Control*, vol. 45, no. 3, pp. 520 - 527, 2000.
- [20] G.J.M. Tuijthof, and J.L. Herder, "Design, actuation and control of an anthropomorphic robot arm," *Mechanism and Machine Theory*, vol. 35, no. 7, pp. 945-962, 2000.
- [21] L. Gaudiller, and F. Matichard, "A Nonlinear Method for Improving the Active Control Efficiency of Smart Structures Subjected to Rigid Body Motions," *IEEE/ASME Trans. on Mechatronics*, vol. 12, no. 5, pp. 542-542-548, 2007.
- [22] C. La-orpacharapan, and L.Y. Pao, "Fast and robust control of systems with multiple flexible modes," *IEEE/ASME Trans. on Mechatronics*, vol. 10, no. 5, pp. 521 -534, 2005.
- [23] R. Caracciolo, A. Trevisani, "Simultaneous rigid-body motion and vibration control of a flexible four-bar linkage," *Mechanism and Machine Theory*, vol. 36, no. 2, pp. 221-243, 2001.
- [24] A. Trevisani, and M.E. Valcher, "An energy-based adaptive control design technique for multibody-mechanisms with flexible links," *IEEE/ASME Trans. on Mechatronics*, vol. 10, no. 5, pp. 571-580, 2005.
- [25] Frisch-Fay, R., *Flexible Bars*, Butterworths, Washington, D.C., 1962.
- [26] P.F. Pai, and A.H. Nayfeh, "A Fully Nonlinear-Theory of Curved and Twisted Composite Rotor Blades Accounting for Warpings and 3-Dimensional Stress Effects," *Int. J. of Solids and Structures*, vol. 31, no. 9, pp. 1309-1340, 1994.
- [27] J. Stoer, and R. Bulirsch, *Introduction to Numerical Analysis*, 2nd, Springer-Verlag, New York, pp. 476-477, 1980.
- [28] P.F. Pai, and A.N. Palazotto, "Large-deformation analysis of flexible beams," *Int. J. of Solids Structures*, vol. 33, no. 9, pp. 1335-1353, 1996.
- [29] J.N. Goodier, "Torsional and flexural buckling of bars of thin-walled open section under compressive and bending loads." *J Appl Mech, ACSE*, vol. 64, 1942.
- [30] S.P. Timoshenko and J.M. Gere, *Theory of elastic stability*, 2nd ed. New York: McGraw-Hill, 1961.
- [31] F.S.M. Jarrar and M.N. Hamdan, "Nonlinear vibrations and buckling of a flexible rotating beam: A prescribed torque approach," *Mechanism and Machine Theory*, vol. 42, no. 8, pp. 919-939, 2007.
- [32] J.L. Batoz and G. Dhatt, "Incremental displacement algorithms for nonlinear problems," *Int. J. Numer. Methods Eng.*, vol. 14, pp. 1262-1267, 1979.
- [33] J.M. Gere, and S.P. Timoshenko, *Mechanics of Material*, 4th ed., PWS Pub. Co, 1997.